Nature Communications

https://doi.org/10.1038/s41467-026-70102-1

Article in Press

Photothermal CO_2 methanation over (NiO/Ru^0)/TiO_2 catalysts via hydrogen spillover

Received: 2 July 2025

Accepted: 9 February 2026

Cite this article as: Nie, Y., Ren, G., Dou, X. *et al.* Photothermal CO_2 methanation over (NiO/Ru^0)/TiO_2 catalysts via hydrogen spillover. *Nat Commun* (2026). https://doi.org/10.1038/s41467-026-70102-1

Yu Nie, Guanhua Ren, Xinyu Dou, Yuan Tang, Donglong Fu, Haoyu Zhang, Chao An, Yanfang Li, Yuchen Guo, Haifeng Wang, Xin Tan, Jinhua Ye, Min Zhou, Tao Yu & Jinlong Gong

Photothermal CO_2 Methanation over (NiO/Ru^0)/TiO_2 Catalysts via Hydrogen Spillover

Yu Nie[a,b,c†], Guanhua Ren[d†], Xinyu Dou[a†], Yuan Tang[b,e], Donglong Fu[a], Haoyu Zhang[a], Chao An[b], Yanfang Li[b], Yuchen Guo[b], Haifeng Wang[d], Xin Tan[b], Jinhua Ye[e,f], Min Zhou[d*], Tao Yu[a*], Jinlong Gong[a,g,h*]

[a]School of Chemical Engineering and Technology, Tianjin University, Tianjin 300350, China
[b]School of Environmental Science and Engineering, Tianjin University, Tianjin 300350, China
[c]China People's Police University, Langfang 065000, People R China
[d]State Key Laboratory of Green Chemical Engineering and Industrial Catalysis, Centre for Computational Chemistry and Research Institute of Industrial Catalysis, East China University of Science and Technology, Shanghai 200237, China
[e]School of Materials Science and Engineering, Tianjin University, Tianjin 300350, China
[f]Research Center for Solar Driven Carbon Neutrality, Hebei University, Baoding 071002, China
[g]International Joint Laboratory of Low-carbon Chemical Engineering of Ministry of Education, Tianjin 300350, China.
[h]Tianjin Normal University, Tianjin 300387, China

[†]These authors contributed equally to this work
E-mail address: yutao@tju.edu.cn (Tao Yu), mzhouccc@ecust.edu.cn (Min Zhou)，jlgong@tju.edu.cn (Jinlong Gong)

Abstract

Photothermal CO_2 methanation presents a promising strategy for mitigating the energy crisis and reducing CO_2 emissions, however, the critical role of hydrogen migration dynamics in addressing reaction kinetics and thermodynamics has not been thoroughly investigated. Here, we demonstrate the design a (NiO/Ru^0)/TiO_2 photothermal catalyst with optimized interfacial architecture and enhanced hydrogen mobility, which facilitates exceptionally selective conversion of CO_2-to-CH_4. Both experimental and theoretical analyses reveal that H_2 dissociates efficiently on Ru^0, subsequently undergoing spillover to O in NiO (O_{NiO}). This process not only redistributes active sites but also influences the reaction kinetics, thereby fundamentally altering the energy landscape associated with CO_2 methanation. Consequently, the

(NiO/Ru^0)/TiO_2 catalyst achieves complete CO_2 conversion and CH_4 selectivity, with a CH_4 production rate of 2552.49 μmol h^{-1} (85.08 mmol g^{-1} h^{-1}) under an irradiation of 25.5 suns without external heat or pressure. This research underscores an innovative engineering approach that leverages hydrogen spillover to enhance photothermal catalytic efficiency and selectivity, thereby providing a robust framework for the advancement of sophisticated photothermal catalysts for selective CO_2 hydrogenation.

Introduction

Carbon dioxide methanation represent a viable strategy for addressing the greenhouse effect and achieving carbon neutrality.[1-3] However, CO_2 methanation is a multi-step surface catalytic reaction involving the synergistic action of multiple intermediates and active sites. That is to say, the process is hindered by sluggish kinetics due to multiple proton-coupled electron transfer steps, which require substantial energy input to activate CO_2 molecules, thereby limiting the overall conversion efficiency.[4] Although the hydrogen spillover (H-spillover) effect has been proposed as a potential means to overcome the kinetic barriers associated with hydrogen activation in CO_2 methanation,[5,6] the underlying dynamic and thermodynamic regulation mechanisms by which H-spillover influences the reaction pathway remain insufficiently understood. One reason is that the mechanism by which H-spillover promotes CO_2 methanation is a complex issue involving multiple steps, scales, and factors. H-spillover may affect the reaction pathway by altering the distribution of surface hydrogen. Additionally, the mechanism of cooperative action between metal sites and carrier sites of H-spillover may be involved in the reaction, and the mechanism of this cooperation needs to be verified systematically.

H-spillover refers to the process in which hydrogen, after undergoing dissociative adsorption and accumulation on a metal catalyst surface, spill into adjacent typically oxides surfaces with relatively low energy barriers.[7-9] [10] This phenomenon enables more precise control over catalytic reaction pathways for more efficient chemical synthesis.[11-13] The increased reactivity associated with H-spillover arises mainly from its dual functionality: (1) providing a rich supply of active hydrogen species for hydrogenating reaction via rapid H_2 dissociation, and (2) accelerating hydrogenation steps in the kinetics.[5,14] In the content of commentary reports regarding H-spillover, Pd/Cu nanomaterials utilize this phenomenon to enhance the selective hydrogenation of alkynes,[15] and Ni nanoparticles improve methane dry reforming

through effective H-spillover.[16] In another case, hydrogen activated by Pd spills over to phosphomolybdate enhances the efficiency of methane oxidation.[17] H-spillover plays a significant role in the hydrogenation of CO_2 to CO.[18] However, the impact of catalyst structure on H-spillover is not yet fully comprehended.[19,20] Consequently, it is imperative to design catalyst structure to modulate the electronic structure, thereby advancing the exploration of the structure-activity relationship between H-spillover and the performance of surface catalytic reactions.

The structural design of catalysts is pivotal in promoting H-spillover during CO_2 methanation. This structural modulation is particularly critical for improving the kinetics of H_2 dissociation and thermodynamically regulating reaction pathways, both of which are essential for hydrogen activation and migration, as well as for the overall efficiency of the CO_2 methanation process.[18,21] Prior studies have demonstrated that reducible catalysts exhibit more pronounced H-spillover effects compared to non-reducible catalysts, given the strong correlation between H-spillover phenomenon and catalyst reducibility .[11,22,23] Although metal Ni remains the predominant choice for facilitating H-spillover due to its cost-effectiveness, from an electronic structure perspective, Ru presents a superior alternative.[24] This is attributed to lower energy barrier for H_2 dissociation, higher surface hydrogen coverage, and enhanced hydrogen migration capabilities of Ru. Among transition metal catalysts, Ru is distinguished by its unique catalytic properties arising from its [Kr]$4d^7 5s^1$ electron configuration. The optimal positioning of its *d*-band center enables an ideal binding strength for hydrogen intermediates ($\Delta G_{H^*} \approx 0$ eV), achieved through a balanced H interaction that avoids both under- and over-binding. These intrinsic electronic characteristics, combined with exceptional capability for H_2 dissociation and dynamic surface properties of Ru, establish it as an excellent candidate for the engineering of H-spillover within catalytic systems.[25-27] In addition to hydrogen activation, the adsorption and activation of CO_2 are equally critical for CO_2 methanation. NiO demonstrates superior capabilities in CO_2 conversion, attributable to Ni^{2+} ([Ar]$3d^8$) possessing a higher *d*-band center (-3.5 eV relative to the Fermi level). The surface of NiO is rich in oxygen atoms and Lewis acid (Ni^{2+}), which facilitate chemical adsorption on basic site (O^{2-}) or interact with Ni^{2+} to form multiple adsorption states, thereby providing abundant pathways for CO_2 activation. This work primary innovation lies in designing a catalyst that optimizes hydrogen dissociation sites beyond those found in Ni-TiO_2 or Ru-TiO_2 systems (**Table S1**), while simultaneously introducing more

effective CO_2 adsorption sites via NiO at activation centers.[1] The energy alignment of the Ni^{2+} *d*-band between metallic Ni and higher oxides optimizes the binding environment, preventing both excessive adsorption and insufficient activation. Serving as a redox-active mediator, NiO plays a vital role in selectively breaking C=O bonds during the CO_2 conversion reaction.[28-30] Furthermore, the presence of high efficient hydrogen dissociation sites is essential for the effective implementation of H-spillover effects.[31] The synergistic combination of Ru and NiO, functioning respectively as sites for hydrogen evolution and terminals for CO_2 alkylation, can substantially enhance the photon-to-electron conversion efficiency of catalytic system by effectively spatially separating and utilizing photogenerated carriers.[32] The development of a composite material comprising Ru and NiO may signify a notable progression in the field of catalytic design for CO_2 hydrogenation. This approach potentially harnesses the synergistic advantages offered by both constituent leveraging components.

This research utilizes an engineered approach to design a photothermal catalyst through the meticulous assembly of NiO and Ru^0 on TiO_2, denoted as NR-TiO_2. TiO_2 is chosen as the engineered support owing to its remarkable stability and tunable support for performance modification. Notably, the compatibility of the matching lattice constants between Ru and TiO_2 facilitates the stabilization and confinement of Ru within the TiO_2 lattice.[33] The adjacent Ru^0 and NiO facilitates an effective channel for H-spillover effect. The hydrogen that is rapidly dissociated at the Ru^0 atoms subsequently spills over to O_{NiO} via the Ru^0–NiO channels, supplying hydrogen for the formation of the hydrocarbon intermediates on NiO. Notably, the spillover of hydrogen from Ru to O_{NiO} on NiO results in the occupation of O_{NiO} sites by hydrogen, which alters the adsorption mode of *COOH from the traditional metal-oxygen (Ni-O_{NiO}) bonding configuration to a dual metal (Ni-Ni) coordination mode, thereby reducing energy barriers associated with C-O bond breaking. The unique structure of the Ru^0–NiO is capable of modulating the reaction pathway for CO_2 methanation on NR-TiO_2, leading to significant enhancements in both conversion rates and selectivity. The photothermal effect induced by Ru^0 and NiO accelerates the transfer of photogenerated carriers and elevates the surface temperature of the catalyst, which synergistically enhances the kinetics of the intermediate hydrogenation process. Notably, H-spillover significantly enhances both thermodynamics and kinetic aspects of CO_2 methanation. This leads to a remarkable conversion rate of approximately 100% for CO_2 and a selectivity of ~100% for CH_4, resulting in a production rate of μmol

h^{-1} (85.08 mmol g^{-1} h^{-1} under an irradiation of 25.5 suns, achieved without the application of external heat or pressure. This study serves as a vital reference for elucidating the role of engineering in facilitating H-spillover, thereby enhancing the efficiency of CO_2 methanation (**Table S2**).

Results and Discussion

Photothermal CO_2 methanation performance

The selectivity and efficiency of CO_2 methanation are influenced by the characteristics of active sites, the efficiency of electron transfer, and the selection of hydrogenation by-products. The effective multiple proton-coupled electron transfer plays a crucial role in determining the reaction rates, energy barriers, and mechanism associated with CO_2 hydrogenation reactions. H-spillover is proposed as a promising strategy to overcome kinetic limitations in CO_2 methanation.[34] The phenomenon of H-spillover necessitates two fundamental conditions: the ability of active metal sites to adsorb H_2 and dissociate them into H atoms, and the presence of a receptor that provides a hydrogen transfer channel and a driving force for hydrogen migration. Informed by a comprehensive understanding of catalyst design strategies, we have meticulously developed a photothermal catalyst comprising NiO, Ru^0 and TiO_2, which possesses the H-spillover effect through an immersion-calcination process (**Fig 1a**). The photothermal catalytic performance was assessed in a sealed system utilizing a glass reactor with a capacity of 358.8 mL, which was thoroughly vacuumed prior to the reaction. To identify the optimal catalyst for subsequent mechanistic investigations, we analyzed the effects of varying loading amount of NiO and Ru^0 on the photothermal catalytic performance. Our findings indicate that the catalytic performance improves progressively with the addition of Ru^0 and NiO (**Fig S1**), with the most significant enhancement observed at a loading of 40 wt.% NiO and 2 wt.% Ru^0 on TiO_2, yielding performance metrics that are 37.7 times and 2.5 times greater than those of synthetic parallel comparison catalysts (**Table S3,** 40 wt.% NiO-1 wt.% Ru^0-TiO_2 and 20 wt.% NiO-2 wt.% Ru^0-TiO_2). The quantity of co-catalyst facilitating the reaction is associated with the efficiency and effectiveness of H-spillover. However, this relationship is not invariably linear with respect to the extent of H-spillover. [35] [36] An excessive amount of co-catalyst may even exert detrimental effects. H-spillover is a multifaceted, multi-step process involving: the dissociation of H_2 molecules on the co-catalyst, migration of H atoms to the interface, occurrence of H-spillover, subsequent

surface migration, and interaction with reactants. The overall rate of H-spillover is governed by the rate-determining step (RDS). While increasing the co-catalyst quantity primarily augments the number of active sites involved in the initial dissociation step, the third step typically serves as RDS.[11] Consequently, an excessive addition of co-catalyst does not proportionally enhance the overall H-spillover process. The optimal loading amounts of NiO and Ru^0, as determined by inductively coupled plasma optical emission spectroscopy (ICP-OES) analysis, were found to be 39.96% and 1.26%, respectively. To further investigate the influence of active sites on the catalytic performance and reaction pathways, 40 wt.% NiO-TiO_2 (designated as N-TiO_2), 2 wt.% Ru^0-TiO_2 (denoted as R-TiO_2), and 40 wt.% NiO-2 wt.%-Ru^0-TiO_2 (denoted as NR-TiO_2) are selected for additional studies.

In the process of photothermal catalysis, the surface temperature of the catalyst is significantly influenced by the intensity of light irradiation, which in turn affects the catalytic performance. As illustrated in **Fig 1b**, **S2** and **S3**, the correlation between increased surface temperature and enhanced catalytic performance due to elevated light intensity exhibits a similar trend across three different catalysts. Notably, NR-TiO_2 demonstrates higher reaction temperatures under photoexcitation compared to N-TiO_2 and R-TiO_2. Specially, it has been observed that the temperature of NR-TiO_2 can reach to 220 ℃ at the light intensity of 2.55 W/cm^2, thereby highlighting the photothermal effect associated with NR-TiO_2. The data points for NR-TiO_2 at 25.5 suns were recorded upon achieving complete conversion. CH_4 was identified as the principal product in photothermal CO_2 hydrogenation, with its concentration increasing over time (**Fig S2**). The CH_4 yields from N-TiO_2, R-TiO_2, and NR-TiO_2 increase with rising light intensity, with NR-TiO_2 achieving the highest rate of CH_4 production. The NR-TiO_2 catalyst demonstrates selectivity above 98%, achieving a peak value of 99.14% at 25.5 suns, surpassing both N-TiO_2 and Ru-TiO_2 across all light intensities examined (**Fig S3**). At a light intensity of 2.55 W/cm^2, the CH_4 evolution rate on NR-TiO_2 reaches an impressive 2552.49 μmol h^{-1}, which is 5.5 and 4.2 times greater than that of N-TiO_2 and R-TiO_2, respectively. This significant enhancement in performance cannot be solely attributed to the mere combination of NiO and Ru^0 components, but rather to specific interfacial interactions occurring at the Ru^0–NiO, which will be discussed in detailed. Simultaneously, in contrast to the temperature variations of TiO_2 under varying light intensities (**Table S4**), the observed temperature elevation in N-TiO_2, R-TiO_2 and NR-TiO_2 indicates that the incorporation of NiO and Ru can significantly

improve the photothermal conversion efficiency of the NR-TiO_2 catalyst. The photothermal conversion efficiency is enhanced, along with specific interfacial interactions at the Ru^0–NiO, which contribute to improved photothermal effect of NR-TiO_2.[37] And this improved photothermal effect is further identified by the performance experiments with different cutoff wavelengths driving the selective CO_2 hydrogenation reaction (**Fig S4**). Cycling tests were performed on the NR-TiO_2 photothermal catalyst at complete conversion as well as within the 20-30% conversion range, along with characterization before and after the reaction confirm the exceptional performance and structural stability of NR-TiO_2 (**Figs S5-S6**).

Previous research has unequivocally demonstrated that, in certain reactions, the photothermal effect serves as the primary driving force,[38] whereas in other reactions, non-thermal effects assume a more prominent role.[39-41] Therefore, it is imperative to differentiate between the thermal and non-thermal effects of NR-TiO_2 in the context of photothermal CO_2 methanation. In this reaction, temperature, light intensity, and wavelength do not independently influence the process; rather, the CH_4 yield results from the interplay of these factors. To elucidate the respective contributions of thermal and non-thermal effects, a series of experiments was performed (**Fig S7-10**). The findings reveal that the photothermal effect predominates under low light intensities, whereas at elevated light intensities, the non-thermal effect gains prominence due to the increased photon flux generating additional hot electrons that facilitate the reaction. Notably, the non-thermal effect is contingent upon both light intensity and temperature, while the thermal effect exhibits greater complexity, being modulated by light intensity, temperature, and catalyst thickness. The rates of CH_4 evolution were measured under conditions both with and without light irradiation. It should be noted that due to the significant temperature increase of the photothermal catalyst NR-TiO_2 under illumination, to achieve comparable experimental conditions, it is necessary to measure the surface temperature of the catalyst under illumination. Here, we employed a thermocouple for temperature measurement, and then maintained the reaction system at the corresponding temperature conditions through electrical heating under non-illuminated conditions. The catalytic performance of NR-TiO_2 when exposed to illumination is markedly superior to the thermal catalytic process conducted without photoexcitation (**Fig 1c**), suggesting that temperature serves a supplementary role in photocatalysis throughout the reaction process. The activation energies for the reactions were determined using the

Arrhenius equation, taking into account the photothermal and thermal properties of CO_2 methanation for N-TiO_2, R-TiO_2, and NR-TiO_2 at their respective temperature (**Fig 1d-e**). Under full spectrum light irradiation (300W Xe lamp), the activation energies for N-TiO_2, R-TiO_2, and NR-TiO_2 are found to be 99.29, 65.85, and 53.96 kJ mol^{-1}, respectively, which are lower than those observed without light irradiation (heated to the corresponding temperature) (104.26, 72.91, and 65.59 kJ mol^{-1}). This reduction in apparent activation energy suggests that specific interactions related to H-spillover at the Ru^0–NiO may effectively lower the activation energy required for CO_2 methanation.

The photothermal catalyst NR-TiO_2 has been theoretically demonstrated to possess the potential for H-spillover effect, which is corroborated by experimental data indicating a marked enhancement in its photothermal performance. Theoretically, the elevated *d*-band center of NiO enhances the activation of CO_2 through π^*-orbital electron injection, thereby weakening C=O bonds. And Ru can being an optimal equilibrium for H^+ adsorption and desorption, promoting efficient H_2 dissociation. Thus, it can be reasonably deduced that the catalytic performance of NR-TiO_2 is intricately linked to the synergistic interplay between NiO and Ru^0, which facilitates rapid H_2 adsorption and dissociation. This is to say that these two components engender a bidirectional charge-transfer platform: Ru swiftly generates active hydrogen species that subsequently spill over to the NiO surfaces, where CO_2 species were pre-activated, which is thoroughly evidenced in the section dedicated to mechanistic analysis. Consequently, NR-TiO_2 demonstrates significant advantages in both photothermal catalytic performance and CH_4 selectivity when compared to currently reported advanced CO_2 methanation catalysts (**Table S5**), further substantiating the effectiveness of our proposed engineering approach to enhance H-spillover effect.

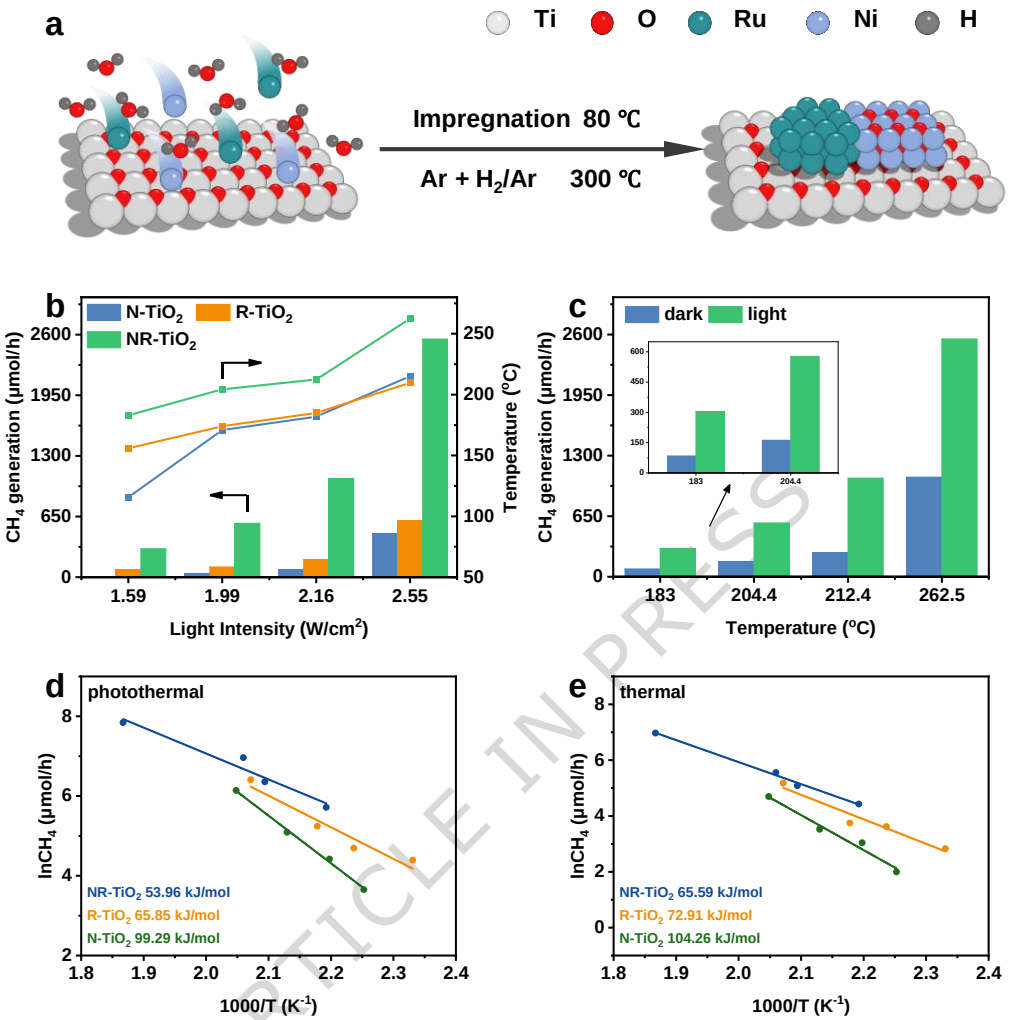

Fig 1. Synthesis, performances and activation energies of photocatalyst. a. Schematic representation of the synthesis process for NR-TiO_2. **b**. Changes in catalyst surface temperature and photothermal CO_2 methanation efficiency of N-TiO_2, R-TiO_2 and NR-TiO_2 under varying light irradiation intensities. **c**. Comparison of thermal CO_2 methanation performance under dark conditions (the surface temperatures of NR-TiO_2 were controlled according to the measured temperature in Fig 1b, illustrated in dark purple) and the photothermal CO_2 methanation performance under light irradiation (illustrated in green). Since the surface temperature of NR-TiO_2 was measured under illumination, the performance comparison in Fig 1c was measured under the same temperature conditions, with the difference being whether photoexcitation was involved in the reaction. **d**. The activation energies associated with photothermal CO_2 methanation for N-TiO_2, R-TiO_2 and NR-TiO_2. **e**. The activation energies for CO_2 methanation on N-TiO_2, R-TiO_2 and NR-TiO_2 under strictly thermal conditions.

Characterization of photothermal catalysts

In order to investigate the correlation between photothermal catalytic performance and the structural characteristics of catalysts, a comprehensive analysis was conducted focusing on crystal structure surface morphology, and electronic coordination information of the catalyst. High Resolution Transmission Electron Microscope (HR-TEM) was employed to ascertain the composition and morphology of the photothermal catalyst. The lattice fringe of TiO_2 is distinctly observed in NR-TiO_2, indicating its high crystallinity (**Fig 2a**), which is further confirmed by X-ray diffraction (XRD) (**Fig 2d**).[42] Specifically, a lattice fringe of 0.214 nm corresponds to the Ru^0(002) crystal plane (JCPDS PDF# 70-0274), while a spacing of 0.209 nm is associated with the NiO(200) plane (JCPDS PDF# 89-7130), thereby confirming the successful synthesis of the NR-TiO_2 composite. The NiO(200) surface displays an alternating arrangement of Ni and O atoms in atomic rows, whereas the Ru(002) surface is characterized by an exposed layer of Ru atoms. This structural arrangement promotes the formation of short-range chemical bonds between the surface Ru atoms and the O atoms from NiO, consequently establishing atomic-scale H-spillover channels. Furthermore, HR-TEM imaging across various regions corroborates the existence of contact among the NiO, Ru^0, and TiO_2 phases (**Figs 2a and S11**). Based on the experimental observations and the findings indicating that the surface energy of NiO(100) is lower than that of compared to NiO(110),[43] a model structure for the NR-TiO_2 has been constructed for Density Functional Theory (DFT) calculations (**Fig S12**). As illustrated in **Fig 2b**, there is a notable accumulation of charge at Ru-NiO, Ru-TiO_2, and NiO-TiO_2, indicating a strong coupling interaction among the three contacted surfaces.

Additionally, the elemental compositions of NR-TiO_2 within a 2μm range were examined utilizing an Energy Dispersive Spectrometer (**Fig 2c**). The results from the scanning images indicate the simultaneous presence of Ru, Ni, Ti, and O, thereby affirming the successful synthesis of the photothermal composite catalyst. The spatial overlap of Ru and Ni observed in the scanning positions is attributed to the interfacial contact between Ru^0 and NiO. Further analyses indicate that the synergistic interaction between the CO_2 activation capability of NiO and the optimized H adsorption-desorption equilibrium of Ru facilitates H-spillover, which addresses the sluggish kinetics of H_2 activation and alleviates the over-stabilization of CO_2. XRD was employed to characterize the phase composition of the photothermal catalyst. The XRD patterns for N-TiO_2, R-TiO_2, and NR-TiO_2 predominantly exhibit diffraction peaks corresponding to TiO_2

(JCPDS PDF#71-1166) (**Fig 2d**). The relatively weak peaks observed for N-TiO_2 and NR-TiO_2 at 37.1º, 43.1º, and 62.6º are attributed to the (111), (200), and (220) planes of NiO (JCPDS PDF# 89-7130).

To elucidate the surface chemical composition of NR-TiO_2, X-ray photoelectron spectroscopy (XPS) was conducted, calibrated at 284.8 eV (C 1*s*). The observed peaks at 854.3 and 872.0 eV correspond to the spin splitting of Ni^{2+}, accompanied by satellite peaks (**Fig 2e**). The binding energy position of Ru^0 is identified at 280.31 eV, while peaks associated with Ti^{4+} are detected at 457.9 eV and 463.57 eV (**Fig S13**). The XPS findings confirm the presence of Ni and Ru on NR-TiO_2 in the forms of NiO and Ru^0, respectively, which is consistent with the results obtained from XRD, HR-TEM, and energy dispersive spectroscopy (EDS) mapping analysis. In comparison to N-TiO_2, the characteristic Ni 2*p* peak in NR-TiO_2 exhibits a shift towards higher binding energy by 0.2 eV, while the binding energy of Ru^0 shifts from 280.31 eV in R-TiO_2 to 280.16 eV in NR-TiO_2. These results indicate that electrons from NiO can be transferred to Ru^0 due to the interfacial contact established between NiO and Ru^0. The light absorption properties of the catalysts play a crucial role in influencing their catalytic activity.[44] To investigate the impact of NiO and Ru^0 on the light absorption characteristic of the catalyst, UV-Vis diffuse reflectance spectroscopy (UV-Vis DRS) was employed. The results indicate that NR-TiO_2 exhibits superior light absorption properties (**Fig S14**), suggesting that the coexistence of NiO and Ru^0 enhances the capture of photon-energy during the energy conversion process, thereby improving the performance of photothermal catalysts.

The electronic structure and coordination characteristic of NR-TiO_2 were examined using X-ray absorption near edge structure (XANES) and extended X-ray absorption fine structure (EXAFS) analyses. As illustrated in **Fig 2f**, the Ni K-edge XANES spectra of NR-TiO_2 exhibit similarities to the NiO standard, however, the absorption edge is observed to shift to higher energies in comparison to the NiO standard. This shift indicates that the average oxidation state of Ni in NR-TiO_2 is elevated relative to the Ni^{2+} state found in the NiO standard.[45,46] The R-space diagrams for NR-TiO_2 reveal that the Ni-O bond length in the first shell layer is 2.03 Å, with a coordination number (N) of 1.0, while the second shell layer exhibits a bond length of 2.98 Å and a coordination number of 6.0 (**Table S6** and **Fig S15a-b**). Notably, the Ni-O bond length in the second shell layer of NR-TiO_2 is shorter than that of the NiO standard, suggesting that robust interfacial interactions significantly decrease the average distance between adjacent Ni and O

atoms. This reduction in bond length is likely to influence the adsorption of *COOH intermediates, thereby facilitating the C-O bond breaking process on Ni.[47] Furthermore, as depicted in **Fig 2g**, the relative intensity and line shape of the Ti K edge peaks in NR-TiO_2 align more closely with the TiO_2 standard, indicating that the TiO_2 in NR-TiO_2 exists in the anatase form, characterized by Ti-O bonds.[48,49] Compared with the TiO_2 standard, the increased intensity of characteristic peaks in NR-TiO_2 is due to the enhanced electron cloud of Ti^{4+} species caused by interfacial interactions, as corroborated by XPS results (**Fig S15c-d**). These findings substantiate that the engineered Ru^0–NiO can significantly influence the resulting interfacial electronic structures and bond lengths, thereby creating favorable conditions for H-spillover to modulate the reaction pathway for photothermal CO_2 methanation.

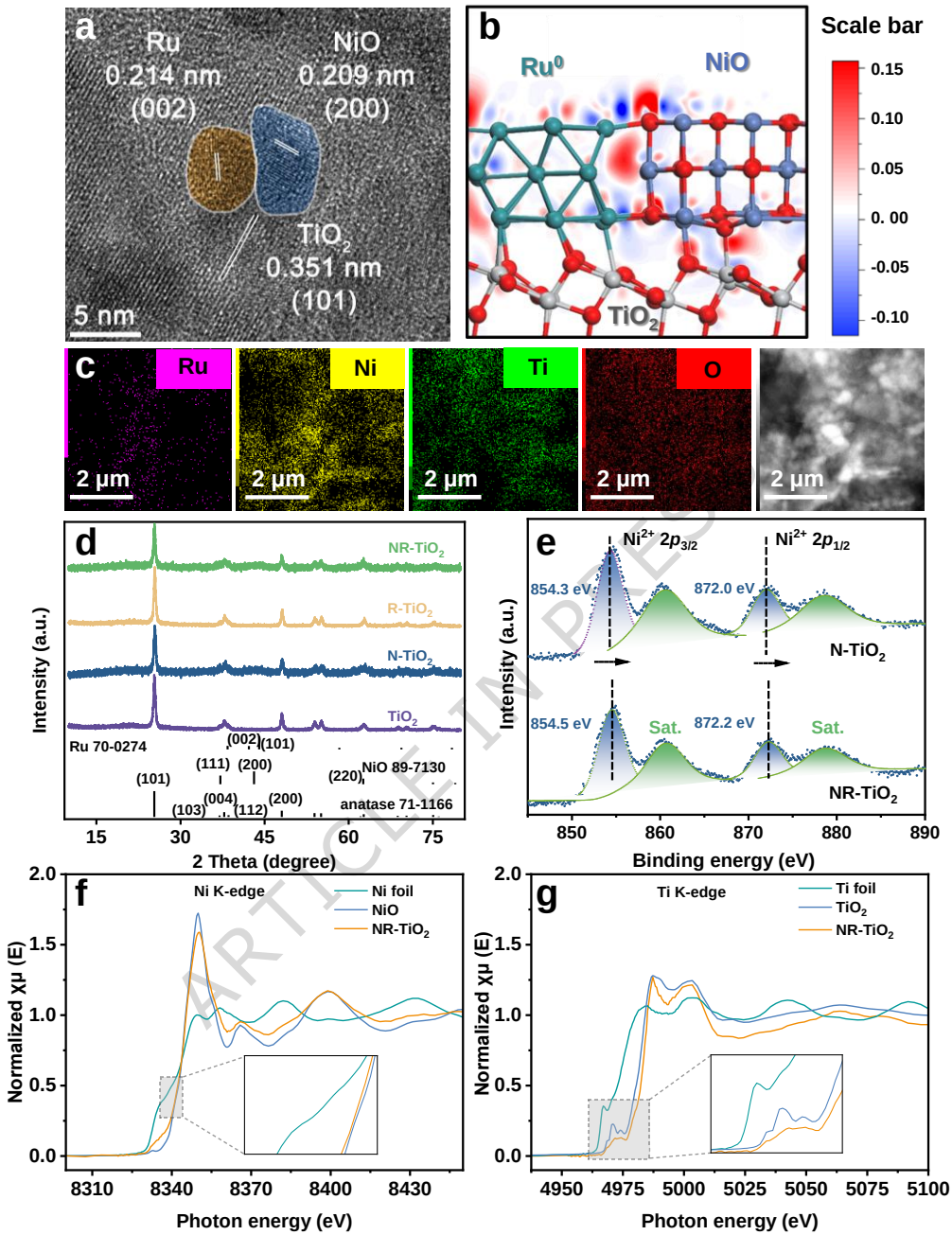

Fig 2. Characterization of morphology and structure of catalysts. a. The HR-TEM image of NR-TiO_2 illustrates the microscopic morphology associated with the interfacial contact among the three phases. **b**. The modeling of the three-phase interfacial structure and the charge density difference of NR-TiO_2. **c**. EDS elemental mapping results for NR-TiO_2 to confirm the uniform distribution of elements and the presence of interfacial contact between NiO and Ru^0. **d**. XRD patterns of the as-synthesized samples to validate the successful synthesis of the catalyst. **e**. High resolution XPS for Ni *2p* on N-TiO_2 and NR-TiO_2 to illustrate the electron shift. **f**. XANES spectra for NR-TiO_2 and reference samples (Ni foil and NiO) at the Ni K-edge. **g**. XANES spectra for NR-TiO_2 and reference samples (Ti foil and TiO_2) at the Ti K-edge.

Separation and transfer of photogenerated carriers

Based on the analysis of CO_2 methanation performance, it is evident that a significant breakthrough has been achieved due to the synergistic effect of thermal effects under photoexcitation conditions and the efficient rapid migration of photogenerated carriers. Consequently, the migration mechanism of these photogenerated carriers is a crucial factor in enhancing the performance of photothermal CO_2 methanation. A comprehensive analysis of the separation and transfer dynamics of these carriers was conducted utilizing photophysical techniques, in-situ characterizations and theoretical evaluations. The directional behavior of photogenerated carriers transfer was elucidated through in-situ XPS and in-situ Kelvin probe force microscopy (KPFM). Initially, in-situ XPS measurements were performed after stabilizing the sample in darkness and subsequently exposing it to light for a duration of 10 minutes. A notable alternation in binding energy of Ni^{2+} within NR-TiO_2 is observed, increasing from 855.9 eV to 856.3 eV (**Fig 3a**), which suggests that Ni is undergoing a chemical state transition characterized by electron loss. Concurrently, the binding energies of Ru^0 and Ti^{4+} are found to decrease by 0.23 eV and 0.1 eV, respectively, under light irradiation, while the binding energy of Ti-O diminishes from 530.12 eV to 530.03 eV, indicating that these three atomic species are situated in an electronically aggregated chemical state[50] (**Fig 3b-d**). Consequently, it is reasonable to deduce that photogenerated electrons migrate from NiO to TiO_2 and Ru^0 upon photoexcitation, thereby establishing NiO as a significant electron donor in the context of photothermal catalysis. To visually assess the migration and accumulation of photoelectrons, in-situ KPFM was employed to examine the variation in surface photo potential across the photocatalysts. Under illumination, NR-TiO_2, N-TiO_2 and R-TiO_2 all demonstrated distinct surface photo potential (SPV) signals, indicative of their light-driven charge transport characteristics. Notably, NR-TiO_2 exhibits the most pronounced reduction in SPV signal (11.03 mV) under illumination (**Fig 3e**) when compared to N-TiO_2 and R-TiO_2 (**Fig S16a, b**), which can be attributed to the surface charge accumulation resulting from the transfer of electrons from the electron donor NiO to Ru^0 and TiO_2. These findings suggest that the incorporation of Ru^0 and NiO enhances the separation and migration of photogenerated carriers on catalyst surfaces, thereby providing the requisite kinetic conditions for the H-spillover effect through the modulation of the interfacial electronic structure.

To elucidate the mechanisms and dynamics underlying the separation of photogenerated carriers, a series of techniques were employed, including photoluminescence spectroscopy (PL), time-resolved photoluminescence spectroscopy (TRPL), transient photocurrent measurements, and electrochemical impedance spectroscopy (EIS). The PL spectrum of N-TiO_2 reveals a peak at 436 nm, which is attributed to the recombination of photogenerated carriers (**Fig 3f**). In comparison to R-TiO_2 and N-TiO_2, NR-TiO_2 exhibits the lowest intensity of the photoluminescence signal, indicating that the incorporation of NiO and Ru^0 effectively inhibits the recombination of photogenerated carriers. This enhancement leads to an increased number of photogenerated carriers and facilitates the kinetics of interfacial charge migration during the photothermal CO_2 methanation reaction. The lifetimes of the photogenerated carriers were assessed through TRPL analysis, revealing that NR-TiO_2 possess the shortest average lifetime, thereby confirming the efficiency of the composite catalyst in promoting the separation and migration of photogenerated carriers. Additionally, transient photocurrent and EIS measurements were performed to further investigate the efficiency of charge separation and transport within the catalysts.[51] The results indicate that NR-TiO_2 achieves the highest photocurrent density and the smallest arc radius, suggesting superior charge separation efficiency and expedited interfacial charge transport compared to N-TiO_2 and R-TiO_2 (**Fig S17**). Consequently, it can be logically inferred that the constructed NR-TiO_2 facilitates efficient separation and migration of photogenerated carriers, thereby enhancing the kinetic properties of the carriers involved in the reaction and establishing favorable conditions for H-spillover modulation of the reaction pathway, ultimately promoting highly selective CO_2 hydrogenation.

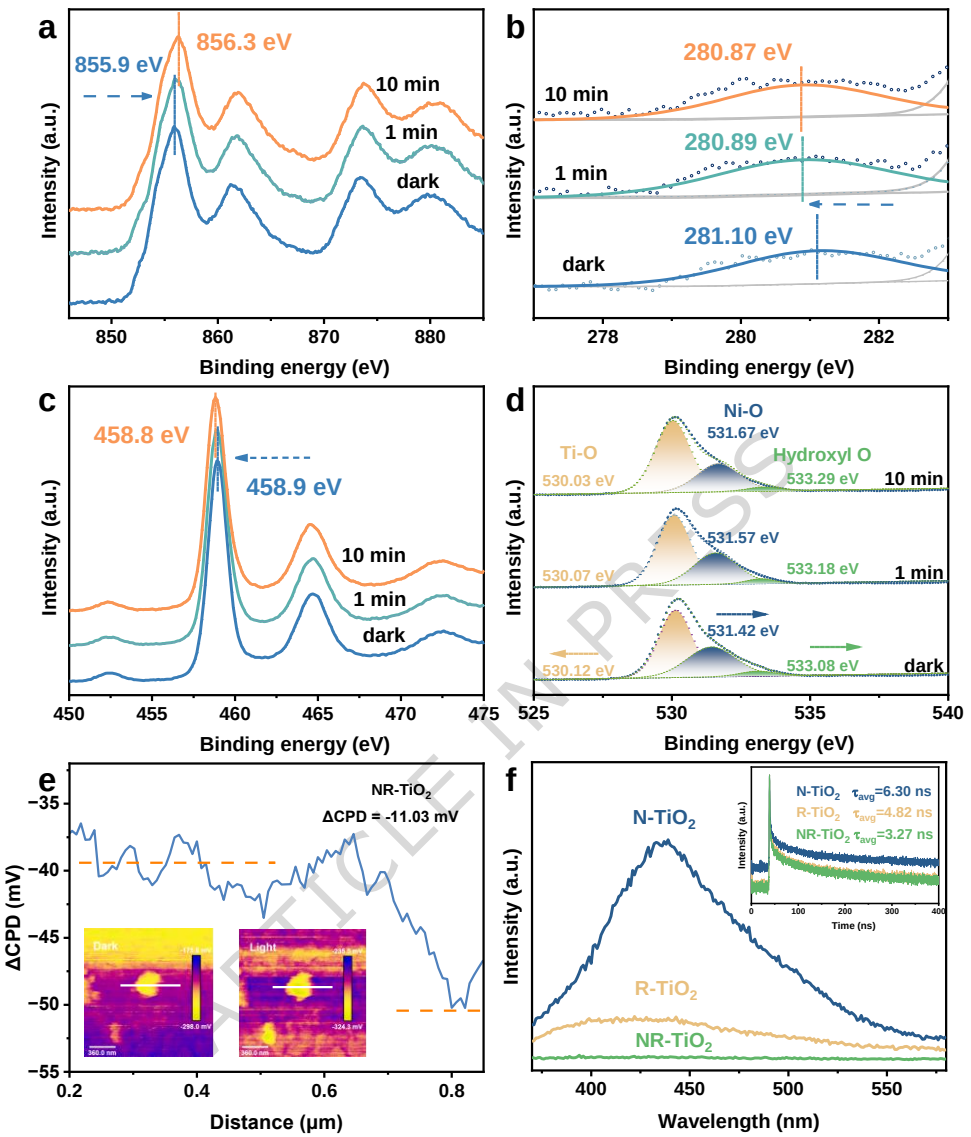

Fig 3.Behaviors of photogenerated carrier transfer. In-situ XPS on **a**. Ni 2*p*, **b**. Ru 3*d*, **c**. Ti 2*p*, and **d**. O 1*s* of NR-TiO_2 both in the absence of light and under light irradiation, the observed differences in binding energy between in-situ XPS and conventional XPS measurements of the same catalysts can be attributed to variations in the instrumentation employed. **e**. The contact potential difference of NR-TiO_2 subtracting the potential measured in dark from that recorded under light conditions (inserts in the Fig illustrating the SPV response of NR-TiO_2 in both dark and illuminated states), the contact potential results of N-TiO_2 and R-TiO_2 measured under the same conditions are presented in Fig S16a and b. **f**. The photoluminescence of characteristics of N-TiO_2, R-TiO_2, and NR-TiO_2 (insert in the Fig depicting the time-resolved photoluminescence of the respective photothermal catalysts).

H-spillover mechanism favoring photothermal CO_2 methanation

In-situ Diffuse Reflectance Infrared Fourier Transform Spectroscopy (DRIFTS) was employed to investigate the alterations in surface chemical bonding on N-TiO_2 and R-TiO_2 during the photothermal CO_2 methanation (**Figs 4a-b**). This analysis elucidates the fundamental mechanisms underlying CO_2 methanation on N-TiO_2 and R-TiO_2. Specifically, for N-TiO_2, the spectral peaks observed at 2349 cm^{-1} and 1837 cm^{-1} are indicative of CO_2 adsorption and the bridged adsorption of $*CO_2^-$. This observation is further supported by vibrational frequency calculations (**Fig S18, S19**). All other computational settings, including the exchange-correlation functional, basis set, k-point sampling, and Hubbard U parameters, were kept consistent with those used in the structural optimizations. And $*CO_2$ adsorption species were detected in CO_2 temperature-programmed desorption (CO_2-TPD) analyses (**Fig S20**). The peak at 1620 cm^{-1} is associated with the carboxy intermediate (*COOH),[52] while the peaks at 1098, 1473 and 1136 cm^{-1} correspond to the intermediates *CHO, $*CH_2O$ and $*CH_3O$, respectively (**Fig 4a**).[52,53] The infrared vibrational peaks of the final product (CH_4) are observed at 1305 cm^{-1} and within the range of 3021-3105 cm^{-1}, indicating the progressive reduction of CO_2 to CH_4.[54] Based on these observations, it is proposed that the CO_2 methanation pathway on N-TiO_2 follows a carboxylate mechanism ($*CO_2 \rightarrow *CO_2^- \rightarrow *COOH \rightarrow *CH_xO \rightarrow *CH_4$). In contrast, the activation of CO_2 on R-TiO_2 occurs through the direct dissociation of the C-O bond, as evidenced by the *CO vibrational peak at 2019 cm^{-1} and the absence of the *COOH peak (**Fig 4b**).[55] The subsequent *CO hydrogenation pathway of *CO to CH_4 on R-TiO_2 is consistent with that observed on N-TiO_2, with no shifts in the peak positions for *CHO, $*CH_2O$, $*CH_3O$, and CH_4. Thus, it can be concluded that CO_2 methanation on R-TiO_2 follows a direct dissociation pathway ($*CO_2 \rightarrow *CO \rightarrow *CH_xO \rightarrow *CH_4$). So far, these findings clearly indicate that the mechanisms of photothermal catalytic CO_2 methanation on N-TiO_2 and R-TiO_2 proceed through two distinct pathways.[56] Meanwhile, in the CO_2 methanation performance analysis (**Fig 1b, c**), NR-TiO_2 exhibited a significant improvement compared to both N-TiO_2 and R-TiO_2, which can be reasonably inferred that there may be critical changes in the reaction mechanism. Therefore, it is necessary to conduct a systematic analysis focusing on the photothermal catalytic CO_2 methanation on NR-TiO_2.

DFT calculations were performed to further clarify the mechanism responsible for the remarkable CO_2 methanation performance of the catalyst. Utilizing HR-TEM images, structural models of the NiO(100)

and $Ru^0(001)$ surfaces were developed (**Fig S21**). Initially, the reaction site for CO_2 methanation was investigated. As illustrated in **Figs S22-25**, the CO_2 molecule is weakly adsorbed on the $Ru^0(001)$ surface through a physisorption mode, exhibiting an adsorption energy of -0.31 eV (**Fig S22**). Subsequently, the generating $*CO_2$ (where * denotes the reaction site) preferentially undergoes direct C-O bond breaking to yield *CO, characterized by a relatively low energy barrier of 0.74 eV and an exothermicity of 0.66 eV (in contrast to the hydrogenation pathway leading to *COOH formation, which has a barrier of 1.07 eV and an endothermicity of 0.26 eV towards, **Fig S23**). This observation is consistent with the favorable direct dissociation pathway identified in the in-situ DRIFTS analysis (**Fig 4b**). The *CO subsequently reacts with hydrogen to produce *CHO, with a barrier of 1.10 eV and an endothermicity of 1.04 eV. The elevated temperatures will facilitate the reaction crossing the high reaction barrier, thereby accelerating the reaction process. This barrier is significantly higher than that for the subsequent hydrogenation of *CHO to form $*CH_xO$ (x=2 and 3) intermediates and the CH_4 product (**Fig S24**). These findings indicate that the $Ru^0(001)$ surface alone demonstrates limited CO_2 methanation activity. Differently, the NiO(100) surface exhibits markedly different catalytic behavior (**Fig S25**). Under elevated temperatures, H_2 adsorption on NiO becomes even less favorable. Although the CO_2 adsorption energy on the bare NiO(100) surface (-0.31 eV) is comparable to that on $Ru^0(001)$, the overall barrier for the kinetically favorable pathway reaches 1.13 eV for *COOH dissociation. Notably, the dissociation barrier for *COOH can be significantly reduced from 1.60 eV to 0.78 eV upon hydrogen coverage on NiO(100), thereby providing compelling evidence that surface hydrogenation, rather than adsorption strength, governs the kinetic feasibility of C-O bond breaking. This underscores the pivotal role of hydrogen in CO_2 methanation, wherein the Ru^0-NiO facilitates H-spillover to synergistically optimize reaction energetics(**Fig 4c**). Under these conditions, the CO_2 adsorption process is enhanced to -0.58 eV (indicating a chemical adsorption mode), and the resulting $*CO_2$ is readily hydrogenated to *COOH with a reduced barrier of 0.46 eV (**Fig S25**). In the subsequent step, *COOH undergoes C-O bond breaking with an exceptionally low barrier of 0.04 eV and is exothermic by -0.29 eV, yielding *CO. This result can be attributed to the alignment of the NiO *d*-band with the π^* antibonding orbitals of CO_2, which promotes electron transfer from the *d*-orbitals of NiO to the antibonding states of CO_2. Such an interaction results in the weakening of the C=O bond through orbital hybridization. The subsequent reduction of *CO to CH_4 proceeds through intermediates

with energy barriers all below 0.28 eV and exhibits exothermicities exceeding 0.46 eV. The observed energy differentials indicate that the NiO(100) surface, rather than Ru^0(001), serves as the primary reaction site for CO_2 methanation in the presence of a sufficient hydrogen source.

While NiO(100) presents kinetic advantages for the CO_2 methanation, it is significantly hindered by its limitations in H_2 dissociation. As illustrated in **Fig 4d**, the H_2 dissociation on NiO(100) encounters a barrier of 0.72 eV and is characterized as endothermic by 0.65 eV, with one H atom adsorbing onto a Ni atom and the other onto an O atom. The elevated thermodynamic energy associated with this process renders H_2 dissociation a critical kinetic bottleneck, which elucidates the susceptibility of Ni-based catalysts to deactivation through mechanisms such as carbon poisoning or sintering.[57] In contrast, H_2 dissociation on the Ru^0(001) surface occurs without an energy barrier and is highly exothermic, underscoring its superior capacity to activate H_2. This disparity in H_2 dissociation capabilities indicates that transfer of hydrogen from Ru^0 to NiO, facilitated by the H-spillover effect, may serve as an effective strategy to enhance CO_2 methanation on NiO(001). The strategic design of NiO and Ru^0 is likely to induce synergistic enhancements in both the kinetics and thermodynamics of photothermal CO_2 methanation.

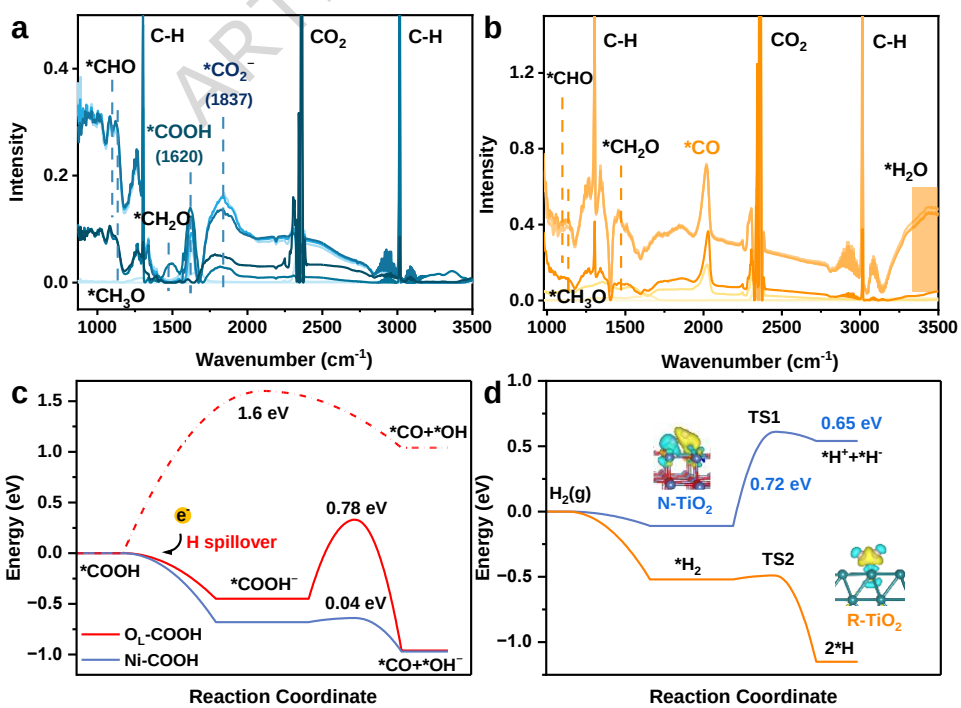

Fig 4. Mechanism of photothermal CO_2 methanation. In-situ DRIFTS on **a**. N-TiO_2 and **b**. R-TiO_2 under photothermal conditions. **c**. Comparison analysis of the energy profiles associated with the C-O bond breaking in the *COOH intermediate. **d**. The energy profiles for heterolytic and homolytic H_2 dissociation on NiO(100) and Ru^0(001). The insets in d. depict the transition states (TS) structures. The yellow and cyan regions denote areas of electron density accumulation and depletion, respectively, with an iso surface value of 0.005 e^-/$Bohr^3$.

To further substantiate this perspective, DFT calculations were conducted to evaluate for H-spillover at the Ru^0–NiO. The simulated NR-TiO_2 model and the corresponding DFT results are depicted in **Figs S12 and 5a**. The adsorption energies of hydrogen on the N-TiO_2 and R-TiO_2 surfaces, both prior to and following interaction, are illustrated in **Fig S26**. It is observed that H exhibited a stronger adsorption affinity for the Ru^0(001) surface compared to the NiO(001) surface, with a notably more negative adsorption energy of -2.88 eV. Consequently, an energy barrier of at least 0.95 eV must be surmounted for hydrogen to transfer from Ru^0(001) to NiO(100). However, upon the establishment of the Ru^0–NiO, the adsorption energy of H on Ru^0(001) significantly decreases, while adsorption on NiO becomes thermodynamically more favorable. Specifically, the hydrogen adsorption energy on Ru^0 in NR-TiO_2 rises to -2.19 eV, whereas on O_{NiO}, it becomes more negative at -2.33 eV. In contrast, the hydrogen adsorption energy on Ni is -1.51 eV, which is 0.82 eV higher than that of O_{NiO}. These findings result in a diminished thermodynamic energy difference of merely -0.14 eV for hydrogen transfer from Ru^0(001) to NiO(100), with the migration target identified as the O_{NiO} on the NiO(100) surface, thus render the process exothermic. The energy barrier for H-spillover is moderate at 0.78 eV (**Fig 5a**), further corroborating the kinetic feasibility of this process, as prior research has indicated that H-spillover becomes thermodynamically unfavorable at energies exceeding 1.15 eV.[11] These results collectively affirm both the kinetic and thermodynamic viability of H-spillover across the Ru^0–NiO. To gain a deep understanding of the H-spillover effect, H_2 temperature-programmed reduction (H_2-TPR) tests were performed on N-TiO_2, R-TiO_2, and NR-TiO_2, respectively. As shown in **Fig 5b**, two reduction peaks are observed for N-TiO_2 at 342.2 ℃ and 463.1 ℃, corresponding to the transitions $Ni^{2+}\rightarrow Ni^{+}$ (α) and $Ni^{+}\rightarrow Ni^{0}$ (β), respectively.[58] The dissociated H atom is generally regarded as possessing a stronger reducing capability than molecular hydrogen. For NR-TiO_2, the reduction peaks of NiO shift to lower temperatures, indicating

that the energy barrier for breaking Ni-O bonds is reduced due to the presence of Ru^0, thereby enhancing the reduction process of Ni through the action of dissociated H atoms. This downward shift in the reduction peaks of NR-TiO_2 provides direct evidence for H-spillover from Ru^0 to NiO. Additionally, the H-spillover in NR-TiO_2 was further corroborated using the WO_3 color reaction, a well-established method for indicating the activation of H_2 at the catalyst (**Fig S27-28**).[59] In this process, WO_3 exhibits challenges in undergoing direct reduction by H_2 at low temperatures. Nevertheless, the incorporation of noble metals facilitates the migration of hydrogen atoms from the metal to the WO_3 lattice via a spillover mechanism, resulting in the formation of hydrogen tungsten bronze H_xWO_3. This transformation is accompanied by a notable color change from yellow to blue. Concurrently, XPS reveal that the appearance of two additional peaks associated with W^{5+} in H_xWO_3.[21] Based on the aforementioned analyses, the structural modeling of the H-spillover process at the Ru^0–NiO is illustrated as **Fig 5c**. The hydrogen exhibits a rapid dissociation from the Ru^0 atom, subsequently spilling over to the O_{NiO} atom, thereby serving as a hydrogen source for the subsequent formation of the $*CH_xO_y$ key intermediates on NiO.

The H-spillover from Ru^0(001) to NiO(100) significantly alters the adsorption behavior of intermediates, as demonstrated by structural and spectroscopic analyses (**Figs 5d, 5e, S18, and S19**). Theoretically, when hydrogen occupies the O_{NiO} due to the H-spillover effect, it induces a notable shift in the *COOH adsorption site from the conventional metal-oxygen (Ni-O_{NiO}) configuration to a bimetallic (Ni-Ni) coordination mode. This reconfiguration leads to a substantial alteration in the vibrational frequency, changing from 1634 cm^{-1} (O_{NiO}-COOH) to 1759 cm^{-1} (Ni-COOH). To further validate the impact of H-spillover effect on the changes in adsorption sites, in-situ DRIFT was conducted. The vibrational peak of *COOH was observed to shift from 1620 cm^{-1} (O_{NiO}-COOH) to 1743 cm^{-1} (Ni-COOH), aligning closely with the theoretical calculations, with the minor discrepancy within an acceptable range for theoretical and practical monitoring. This observed shift in the vibrational frequency of *COOH from in-situ DRIFT spectral changes provide direct evidence for the reconfiguration process. The alternation of *COOH adsorption sites facilitate the C-O bond breaking, significantly decreasing the dissociation barrier of *COOH from 0.78 eV to 0.04 eV, thereby underscoring the role of H-spillover in promoting C-O bond breaking through the reconfiguration of intermediate coordination (**Fig 4c**). Notably, the occupation of O atom by hydrogen further reduces the barrier of this reaction process to 0.78 eV,

accompanied by an enthalpy change of -0.73 eV. The consistent frequency shift consistent from the transition of O_{NiO}-COOH adsorption to Ni-COOH as a consequence of H-spillover highlights the enhancement of catalytic activity of NR-TiO_2 for CO_2 methanation.

The analysis presented above systematically delineates the reaction mechanism underlying the H-spillover effect that facilitates CO_2 methanation, which can be encapsulated in two fundamental processes: (1) the H-spillover from Ru^0 to O_{NiO} circumvents the energy barrier associated with hydrogen dissociation on the NiO surface, thereby supplying an adequate hydrogen source for the CO_2 methanation reaction, (2) the accumulation of H on the NiO surface effectively modulates the bidentate adsorption sites of the intermediate *COOH, resulting in a fundamental alteration in the kinetics of C-O bond breaking. Consequently, a mechanism has been proposed to elucidate how the H-spillover effect influences the adsorption configuration of key intermediates *COOH, thereby regulating reaction pathways and enhancing the efficiency of CO_2 methanation (**Figs 5f and S29**). Initially, H_2 dissociates rapidly on the Ru^0(001) surface and subsequently spills over onto the NiO(100)surface, providing a substantial hydrogen source for CO_2 methanation on NiO(100). The H-spillover effect results in the occupation of O_{NiO} in NiO by H, which alters the bidentate adsorption of *COOH from Ni-O_{NiO} sites to Ni-Ni sites, significantly lowering the energy required for C-O bond breaking. The CO_2 methanation pathway comprises a series of hydrogenation steps, wherein the H-spillover from Ru^0 to O_{NiO} dynamically influences the reaction energetics. This directional H-spillover leads to specific reactions in energy barriers for individual steps, while the H-spillover at the Ru^0–NiO enhanced proton-transfer kinetics, as demonstrated by in situ DRIFT and DFT calculations. Collectively, the H-spillover effect on sequential hydrogenation processes over NR-TiO_2 results in a 37.7-fold increase in CH_4 formation efficiency compared to the H-spillover-free N-TiO_2 catalyst. Furthermore, the H-spillover effect facilitates the breaking of the C-O bond, yielding the *CO intermediate, which is subsequently hydrogenated to produce CH_4. Through the H-spillover effect at the Ru^0–NiO, CO_2 is effectively converted into CH_4, achieving atomic-scale regulation of CO_2 methanation within the NR-TiO_2 system.

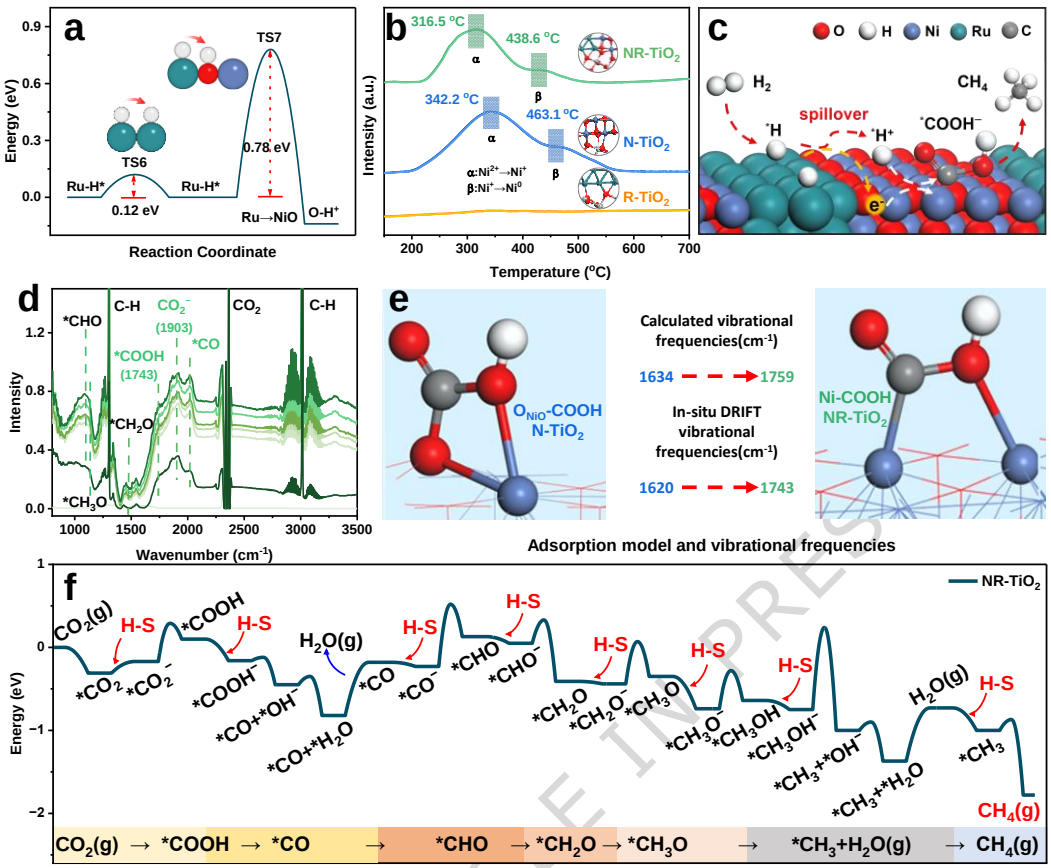

Fig 5. Mechanism of H-spillover effect on photothermal CO_2 methanation. a. The energy profile associated with H-spillover on NR-TiO_2. **b**. H_2-TPR analysis of N-TiO_2, R-TiO_2 and NR-TiO_2. **c**. Schematic representations illustrating H-spillover on NR-TiO_2. **d**. In-situ DRIFTS of CO_2 methanation on NR-TiO_2 under photothermal conditions. **e**. The adsorption model along with the vibrational frequencies of *COOH on N-TiO_2 and NR-TiO_2. **f**. The energy profile of CO_2 methanation reaction on NR-TiO_2

This paper describes the meticulously designed Ru^0–NiO facilitating photothermal CO_2 methanation via hydrogen spillover. The dissociation of H_2 at the Ru^0 generates a sufficient supply of hydrogen for CO_2 methanation, thereby accelerating the kinetics of the CO_2 methanation process. This distinctive Ru^0–NiO establishes a unique reaction pathway influenced by H-spillover. Specifically, the spill over of hydrogen from Ru^0 to the NiO surface preferentially occupies the O_{NiO}, resulting in a shift of the intermediate adsorption site from Ni-O_{NiO} to Ni-Ni, which lower the energy barrier associated with C-O bond breaking during CO_2 methanation. Comprehensive characterizations and theoretical analyses clarify the fundamental mechanism of CO_2 methanation mechanism on the catalyst surface, affirming the critical role of H-spillover in supplying robust hydrogen for CO_2 hydrogenation on the NiO surface, as well as the synergistic effect of adaptable reaction sites in modulating the reaction pathway. These findings underscore the potential of H-spillover effect to synergistically influence the kinetics and reaction pathways involved in CO_2 conversion.

Methods

Experimental Section

Materials. $RuCl_3 \cdot 3H_2O$ (99.95%, Heowns), Na_2CO_3 (98%, Tianjin Jiangtian Chemistry), P25 TiO_2(AR, Degussa), and $NiCl_3 \cdot 6H_2O$ (AR, Tianjin Sanchang Chemistry), all of which were employed without additional purification.

Preparation of catalyst.300 mg P25 was added into 30 mL DI water, followed by the addition of 488 mg $NiCl_2$ and 480 μL of an aqueous $RuCl_3$ (25 mg mL^{-1}) solution. The pH of mixture was subsequently adjusted to 8 using a Na_2CO_3 solution (1.2M). The resulting solution was then placed in a water bath at 80 ℃ for a duration of 12 h. The precipitate was washed for three times and dried at 120 ℃ for 12 h. The dried products were ground and subjected to calcination in a tube furnace, following a temperature ramp of 10 ℃ min^{-1} until reaching 300 ℃, where they were calcined for 1 h in an Ar atmosphere, followed by an additional hour in a H_2/Ar mixture. This resultant sample was designated as NR-TiO_2. The N-TiO_2 and R-TiO_2 samples were synthesized without the inclusion of $RuCl_3$ and $NiCl_2$, respectively. Variations in the ratios of Ni and Ru were achieved by modifying the quantities of $NiCl_2$ and $RuCl_3$ (either doubling or halving their amounts). The samples were according labeled as 20 wt.% NiO-2 wt.% Ru^0-TiO_2 (with

halved $NiCl_2$), 80 wt.% NiO-2 wt.% Ru^0-TiO_2 (with doubled $NiCl_2$), 40 wt.% NiO-1 wt.% Ru^0-TiO_2 (with halved $RuCl_3$) and 40 wt.% NiO-4 wt.% Ru^0-TiO_2 (with doubled $RuCl_3$).

Photothermal CO_2 methanation test

Photothermal CO_2 methanation was conducted with a sealed system utilizing a glass reactor with capacity of 358.8 mL, which was thoroughly evacuated prior the initiation of the reaction. During the experimental procedures, 30 mg catalyst was meticulously ground and uniformly dispersed onto quartz paper, while 50 mg catalyst was employed in cycling experiments. Following the vacuum process, 1.6 mmol high purity absolute CO_2 and 6.4 mmol H_2 were introduced into the system and allowed to adsorb in the dark for a duration of 30 min. A full spectrum 300W Xe lamp served as the light source, complemented by a compound eye lens and a Fourier lens to mitigate temperature discrepancies.[60] The incorporation of a homogenizer modified the beam path, ensuring an even distribution of light across the catalyst surface, thereby enhancing the precision of the temperature measurements and preventing the underestimation of temperature that could occur if the beam was not uniformly distributed at the measurement point. To evaluate the respective contributions of thermal and non-thermal effects in the reaction, a reactor with adjustable external heating temperature was utilized. By systematically varying both the light intensity and the reaction temperature, the non-thermal effects of NR-TiO_2 in the photothermal CO_2 methanation were extracted. A GC-2014 gas chromatograph was employed to analyzed the concentrations of CH_4, CO, CO_2, C_2H_4, C_2H_6 and H_2 on an hourly basis. Organic compounds were separated using a Sunpak-A (H-2099, 50-80) column, while CO and CO_2 were separated on a Porapak-QS (H-2100, 80-100) column after passing through a methane conversion furnace. H_2 was separated using a 5A molecular sieve column. The detection of organic compounds and CO was performed using a hydrogen flame ionization detector (FID), while a thermal conductivity detector (TCD) was utilized for H_2. The conversion of CO_2 was calculated using Equation (1):

Eq. (1) $$CO_2 \text{ conversion} = \frac{CO_2 \text{ initial} - CO_2 \text{ eventual}}{CO_2 \text{ initial}}$$

The selectivity of CH_4 was determined using Equation (2):

Eq. (2) $$CH_4 \text{ selectivity} = \frac{CH_4 \text{ yield}}{CO \text{ yield} + CH_4 \text{ yield} + C_2H_4 \text{ yield} + C_2H_6 \text{ yield}}$$

Characterizations

X-ray diffraction (XRD) analysis, utilizing a Cu Kα radiation source and conducted with a D8-Focus instrument from Bruker (Germany), was employed to elucidate the crystal structures of the samples. In-situ diffuse reflectance infrared Fourier transform spectroscopy (DRIFTS) was performed using an Invenio-S instrument. The concentration of metal ions was determined through inductively coupled plasma optical emission spectrometry (ICP-OES) with an iCAP7000 series instrument from Thermo. The chemical compositions of the samples were analyzed via X-ray photoelectron spectroscopy (XPS) using a Thermo Scientific Escalab 250XI apparatus. The morphological characteristics of the samples was examined using transmission electron microscopy (TEM) with a JEM-F200 instrument from Japan. Energy dispersive spectroscopy (EDS) analysis focused on the Ni K, Ru L, Ti K, and O K peaks. The atomic coordination environment was analyze using X-ray Absorption Fine Structure (XAFS) with a Table XAFS-500-A system. In-situ XPS measurements was conducted with by the Thermo Escalab 250Xi (Thermo Fisher, USA). The light absorption spectra were derived from the ultraviolet-visible diffuse reflectance spectra (UV-vis DRS), measured with UV-3600 spectrophotometer from Shimadzu (Japan). Photoluminescence (PL) properties were investigated using a fluorescence spectrophotometer (Fluorolog-3, HORIBA Scientific, USA) with an excitation wavelength of 320 nm, and the time-resolved photoluminescence (TRPL) lifetime was calculated as detailed in Text. S1. Furthermore, the samples were deposited on an indium tin oxide (ITO) conducting glass for photoelectrochemical measurements, with further details provided in Text S2. CO_2 temperature-programmed desorption (CO_2-TPD) and H_2 temperature-programmed reduction (H_2-TPR) were conducted using an AutoChem II 2920 chemisorption instrument.

Data Availability

All data supporting the findings of this work are available in the Manuscript and Supplementary information. The source data generated in this study are provided in the Source Data file. Source data are provided with this paper. All data are available from the corresponding author upon request

References

1 Li, Q. *et al.* Disclosing support-size-dependent effect on ambient light-driven photothermal CO_2 hydrogenation over nickel/titanium dioxide. *Angewandte Chemie-International Edition* **63**, e202318166, doi:10.1002/anie.202318166 (2024).

2 Wang, S. H. *et al.* Grave-to-cradle upcycling of Ni from electroplating wastewater to photothermal CO_2 catalysis. *Nature Communications* **13**, 5305, doi:10.1038/s41467-022-33029-x (2022).

3 Mateo, D. *et al.* Efficient visible-light driven photothermal conversion of CO_2 to methane by nickel nanoparticles supported on barium titanate. *Advanced Functional Materials* **31**, doi:10.1002/adfm.202008244 (2021).

4 Zhu, X. L. *et al.* Supercharged CO_2 photothermal catalytic methanation: high conversion, rate, and selectivity. *Angewandte Chemie-International Edition* **62**, e202218694, doi:10.1002/anie.202218694 (2023).

5 Guo, Y. *et al.* Low-temperature CO_2 methanation over CeO_2-supported Ru single atoms, nanoclusters, and nanoparticles competitively tuned by strong metal-support interactions and H-spillover effect. *ACS Catalysis* **8**, 6203-6215, doi:10.1021/acscatal.7b04469 (2018).

6 Tan, Z. H., Chen, J. & Lin, S. Theoretical insights into H_2 activation and hydrogen spillover on near-surface alloys with embedded single Pt atoms. *ACS Catalysis* **14**, 2194-2201, doi:10.1021/acscatal.3c05660 (2024).

7 Jiang, L. Z. *et al.* Facet engineering accelerates spillover hydrogenation on highly diluted metal nanocatalysts. *Nature Nanotechnology* **15**, 848-853, doi:10.1038/s41565-020-0746-x (2020).

8 Gu, K. X. & Lin, S. Sustained hydrogen spillover on Pt/Cu(111) single-atom alloy: dynamic insights into gas-induced chemical processes. *Angewandte Chemie-International Edition* **62**, e202312796, doi:10.1002/anie.202312796 (2023).

9 Shen, C. Y. *et al.* CO_2 hydrogenation to methanol on indium oxide-supported rhenium catalysts: the effects of size. *ACS Catalysis* **12**, 12658-12669, doi:10.1021/acscatal.2c03709 (2022).

10 Li, X. Y. *et al.* Controlling CO_2 hydrogenation selectivity by metal-supported electron transfer. *Angewandte Chemie-International Edition* **59**, 19983-19989, doi:10.1002/anie.202003847 (2020).

11 Karim, W. *et al.* Catalyst support effects on hydrogen spillover. *Nature* **541**, 68-71, doi:10.1038/nature20782 (2017).

12 Wang, S. Z., Zhang, K., Li, H., Xiao, L. P. & Song, G. Selective hydrogenolysis of catechyl lignin into propenylcatechol over an atomically dispersed ruthenium catalyst. *Nature Communications* **12**, 416, doi:10.1038/s41467-020-20684-1 (2021).

13 Yin, H. *et al.* Nanometre-scale spectroscopic visualization of catalytic sites during a hydrogenation reaction on a Pd/Au bimetallic catalyst. *Nature Catalysis* **3**, 834-842, doi:10.1038/s41929-020-00511-y (2020).

14 Parastaev, A. *et al.* Boosting CO_2 hydrogenation via size-dependent metal-support interactions in cobalt/ceria-based catalysts. *Nature Catalysis* **3**, 526-533, doi:10.1038/s41929-020-0459-4 (2020).

15 Jiang, L. Z. *et al.* Facet engineering accelerates spillover hydrogenation on highly diluted metal nanocatalysts. *Nature Nanotechnology* **15**, 848-+, doi:10.1038/s41565-020-0746-x (2020).

16 Zhu, Q. Y. *et al.* Enhanced CO_2 utilization in dry reforming of methane achieved through nickel-mediated hydrogen spillover in zeolite crystals. *Nature Catalysis* **5**, 1030-1037, doi:10.1038/s41929-022-00870-8 (2022).

17 Wang, S. K. *et al.* H_2-reduced phosphomolybdate promotes room-temperature aerobic oxidation of methane to methanol. *Nature Catalysis*, doi:10.1038/s41929-023-01011-5 (2023).

18 Kang, H. *et al.* Generation of oxide surface patches promoting H-spillover in Ru/(TiO_x)MnO catalysts enables CO_2 reduction to CO. *Nature Catalysis* **6**, 1062-1072, doi:10.1038/s41929-023-01040-0 (2023).

19 Hulsey, M. J., Fung, V., Hou, X., Wu, J. & Yan, N. Hydrogen spillover and its relation to hydrogenation: observations on structurally defined single-atom sites. *Angewandte Chemie-International Edition* **61**, e202208237, doi:10.1002/anie.202208237 (2022).

20 Xiong, M., Gao, Z. & Qin, Y. Spillover in heterogeneous catalysis: new insights and opportunities. *ACS Catalysis* **11**, 3159-3172, doi:10.1021/acscatal.0c05567 (2021).

21 Yang, J. J. *et al.* Atomically dispersed Pt and NiO clusters synergistically enhanced C-O bond hydrogenolysis. *CCS Chemistry* **6**, 709-718, doi:10.31635/ccschem.024.202303240 (2024).

22 Tan, M. W. *et al.* Hydrogen spillover assisted by oxygenate molecules over nonreducible oxides. *Nature Communications* **13**, 1457, doi:10.1038/s41467-022-29045-6 (2022).

23 Mahdavi-Shakib, A. *et al.* The role of surface hydroxyls in the entropy-driven adsorption and spillover of H_2 on Au/TiO_2 catalysts. *Nature Catalysis* **6**, 710-719, doi:10.1038/s41929-023-00996-3 (2023).

24 Li, X. *et al.* Boosting fischer–tropsch synthesis via tuning of N dopants in TiO_2@CN-supported Ru catalysts. *Transactions of Tianjin University* **30**, 90-102, doi:10.1007/s12209-024-00382-5 (2024).

25 Wu, S. S. *et al.* Rapid interchangeable hydrogen, hydride, and proton species at the interface of transition metal atom on oxide surface. *Journal of the American Chemical Society* **143**, 9105-9112, doi:10.1021/jacs.1c02859 (2021).

26 Shen, H. J., Wu, X. Y., Jiang, D. H., Li, X. N. A. & Ni, J. Identification of active sites for hydrogenation over Ru/SBA-15 using *in situ* fourier-transform infrared spectroscopy. *Chinese Journal of Catalysis* **38**, 1597-1602, doi:10.1016/s1872-2067(16)62571-8 (2017).

27 Yang, C. Y. *et al.* Intrinsic mechanism for carbon dioxide methanation over Ru-based nanocatalysts. *ACS Catalysis* **13**, 11556-11565, doi:10.1021/acscatal.3c02502 (2023).

28 Ghaemi, A., Mashhadimoslem, H. & Zohourian Izadpanah, P. NiO and MgO/activated carbon as an efficient CO_2 adsorbent: characterization, modeling, and optimization. *International Journal of Environmental Science and Technology* **19**, 727-746, doi:10.1007/s13762-021-03582-x (2022).

29 Medina, O. E., Amell, A. A., López, D. & Santamaría, A. Comprehensive review of nickel-based catalysts advancements for CO_2 methanation. *Renewable & Sustainable Energy Reviews* **207**, 114926, doi:10.1016/j.rser.2024.114926 (2025).

30 Raziq, F. *et al.* Isolated Ni atoms enable near-unity CH_4 selectivity for photothermal CO_2 hydrogenation. *Journal of the American Chemical Society* **146**, 21008-21016, doi:10.1021/jacs.4c05873 (2024).

31 Xie, L. J., Liang, J. S., Jiang, L. Z. & Huang, W. Effects of oxygen vacancies on hydrogenation efficiency by spillover in catalysts. *Chemical Science* **16**, 3408-3429, doi:10.1039/d4sc07375d (2025).

32 Guo, C. *et al.* Enhanced photo-thermal CO_2 methanation with tunable Ru_xNi_{1-x} catalytic sites: alloying beyond pure Ru. *Advanced Functional Materials* **35**, doi:10.1002/adfm.202414931 (2025).

33 Zhou, Y. Y. *et al.* Lattice-confined Ru clusters with high CO tolerance and activity for the hydrogen oxidation reaction. *Nature Catalysis* **3**, 454-462, doi:10.1038/s41929-020-0446-9 (2020).

34 Shen, C. Y., Liu, M. H., He, S., Zhao, H. B. & Liu, C. J. Advances in the studies of the supported ruthenium catalysts for CO_2 methanation. *Chinese Journal of Catalysis* **63**, 1-15, doi:10.1016/s1872-2067(24)60090-2 (2024).

35 Jiang, L. *et al.* Facet engineering accelerates spillover hydrogenation on highly diluted metal nanocatalysts. *Nature Nanotechnology* **15**, 848-853, doi:10.1038/s41565-020-0746-x (2020).

36 Wang, N. L. *et al.* Spillover hydrogen boosts nitroarene hydrogenation to industrial activity with ppm-level platinum single atoms. *Angewandte Chemie-International Edition*, e202514332, doi:10.1002/anie.202514332 (2025).

37 Bian, X. A., Zhao, Y., Zhou, C. & Zhang, T. Minimizing temperature bias through reliable temperature determination in gas-solid photothermal catalytic reactions. *Angewandte Chemie-International Edition* **62**, e202219340, doi:10.1002/anie.202219340 (2023).

38 Li, X., Zhang, X., Everitt, H. O. & Liu, J. Light-induced thermal gradients in ruthenium catalysts significantly enhance ammonia production. *Nano Letters* **19**, 1706-1711, doi:10.1021/acs.nanolett.8b04706 (2019).

39 Zhang, X. *et al.* Plasmon-enhanced catalysis: Distinguishing thermal and nonthermal effects. *Nano Letters* **18**, 1714-1723, doi:10.1021/acs.nanolett.7b04776 (2018).

40 Dubi, Y., Un, I. W. & Sivan, Y. Thermal effects-An alternative mechanism for plasmon-assisted photocatalysis. *Chemical Science* **11**, 5017-5027, doi:10.1039/C9SC06480J (2020).

41 Li, X., Everitt, H. O. & Liu, J. Confirming nonthermal plasmonic effects enhance CO_2 methanation on Rh/TiO_2 catalysts. *Nano Research* **12**, 1906-1911, doi:10.1007/s12274-019-2457-x (2019).

42 Saraev, A. A. *et al.* Cu/TiO_2 photocatalysts for CO_2 reduction: Structure and evolution of the cocatalyst active form. *Transactions of Tianjin University* **30**, 140-151, doi:10.1007/s12209-024-00384-3 (2024).

43 Xiang, J. X., Xiang, B. & Cui, X. D. NiO nanoparticle surface energy studies using first principles calculations. *New Journal of Chemistry* **42**, 10791-10797, doi:10.1039/c8nj00457a (2018).

44 Yang, Z. W. *et al.* Optically selective catalyst design with minimized thermal emission for facilitating photothermal catalysis. *Nature Communications* **15**, 7599, doi:10.1038/s41467-024-51896-4 (2024).

45 Sayago, D. I. *et al.* Bond lengths and bond strengths in weak and strong chemisorption: N_2, CO, and CO/H on nickel surfaces. *Physical Review Letters* **90**, 116104, doi:10.1103/PhysRevLett.90.116104 (2003).

46 Zhu, J. B. *et al.* Quasi-covalently coupled Ni-Cu atomic pair for synergistic electroreduction of CO_2. *Journal of the American Chemical Society* **144**, 9661-9671, doi:10.1021/jacs.2c00937 (2022).

47 Wei, X. Q. *et al.* Switching product selectivity in CO_2 electroreduction via Cu-S bond length variation. *Angewandte Chemie-International Edition* **63**, e202409206, doi:10.1002/anie.202409206 (2024).

48 Wang, Y. *et al.* Rational design of defect metal oxide/covalent organic frameworks Z-scheme heterojunction for photoreduction CO_2 to CO. *Applied Catalysis B-Environment and Energy* **327**, doi:10.1016/j.apcatb.2023.122419 (2023).

49 Zhao, Y. F. *et al.* Ultrafine NiO nanosheets stabilized by TiO_2 from monolayer NiTi-LDH precursors: an active water oxidation electrocatalyst. *Journal of the American Chemical Society* **138**, 6517-6524, doi:10.1021/jacs.6b01606 (2016).

50 Chen, C. *et al.* Supported Au single atoms and nanoparticles on MoS_2 for highly selective CO_2-to-CH_3COOH photoreduction. *Nature Communications* **15**, doi:10.1038/s41467-024-52291-9 (2024).

51 Zhu, Y. F. *et al.* Hierarchical nanoporous Cu_6Sn_5/Sn heterojunction with accelerated CO_2 protonation for formate production. *Transactions of Tianjin University* **31**, 411-420, doi:10.1007/s12209-025-00446-0 (2025).

52 Liu, P. G. *et al.* Synergy between palladium single atoms and nanoparticles via hydrogen spillover for enhancing CO_2 photoreduction to CH_4. *Advanced Materials* **34**, e2200057, doi:10.1002/adma.202200057 (2022).

53 Yi, J. D. *et al.* Highly selective CO_2 electroreduction to CH_4 by in situ generated Cu_2O single-type sites on a conductive MOF: stabilizing key intermediates with hydrogen bonding. *Angewandte Chemie-International Edition* **59**, 23641-23648, doi:10.1002/anie.202010601 (2020).

54 Millet, M. M. *et al.* Ni single atom catalysts for CO_2 activation. *Journal of the American Chemical Society* **141**, 2451-2461, doi:10.1021/jacs.8b11729 (2019).

55 Wang, C. T. *et al.* Product selectivity controlled by nanoporous environments in zeolite crystals enveloping rhodium nanoparticle catalysts for CO_2 hydrogenation. *Journal of the American Chemical Society* **141**, 8482-8488, doi:10.1021/jacs.9b01555 (2019).

56 Jia, J.-Y. *et al.* Review of iron-based catalysts for carbon dioxide fischer–tropsch synthesis. *Transactions of Tianjin University* **30**, 178-197, doi:10.1007/s12209-024-00392-3 (2024).

57 Li, S. & Gong, J. Strategies for improving the performance and stability of Ni-based catalysts for reforming reactions. *Chemical Society Reviews* **43**, 7245-7256, doi:10.1039/c4cs00223g (2014).

58 Wang, C. X. *et al.* Hydroxylated TiO_2-induced high-density Ni clusters for breaking the activity-selectivity trade-off of CO_2 hydrogenation. *Nature Communications* **15**, 8290, doi:10.1038/s41467-024-52547-4 (2024).

59 Khoobiar, S. Particle to particle migration of hydrogen atoms on platinum—alumina catalysts from particle to neighboring particles. *The Journal of Physical Chemistry* **68**, 411-412 (1964).

60 Bian, X. N., Zhao, Y. X., Zhou, C. & Zhang, T. R. Minimizing temperature bias through reliable temperature determination in gas-solid photothermal catalytic reactions. *Angewandte Chemie-International Edition* **62**, doi:10.1002/anie.202219340 (2023).

Acknowledgements

This work was supported by the National Key Research and Development Program of China (2021YFA1500700, 2021YFA1500704), the National Natural Science Foundation of China (22121004, 22038009, 22250008, 22361142838), the National Natural Science Foundation of China (22372116), the China Postdoctoral Science Foundation Funded Project (Grant 2024M760908), and China People's Police University: University-Level General Research Project-Doctoral Research Innovation Program Project (BSKYZX202433).

Author Contributions Statement

T.Y. established the research line and supervised the current work; M.Z. and J.G. co-supervised the current work; Y.N. performed the experiments, data analysis, and wrote the manuscript; G.R. offered theoretical calculations and wrote the manuscript; X.D. performed the experiments and data analysis. D.F., H.W., X.T. and J.Y. provided resources; Y.T., H.Z. C.A., Y.L. and Y.G. were involved in the analysis of data and revised the manuscript. All the authors reviewed, approved, and contributed to the final version of the manuscript.

Competing Interests Statement

The authors declare no competing interests.

Editorial summary:

Using sunlight to turn carbon dioxide into fuels is appealing, but reactions are often inefficient. This study shows a photothermal catalyst that lets hydrogen move between sites, enabling selective conversion of carbon dioxide to methane.

Peer Review Information: *Nature Communications* thanks Josep Albero and the other, anonymous, reviewer(s) for their contribution to the peer review of this work. A peer review file is available.